Jagannath University Journal of Science
Volume 11, Number I, Jun. 2024, pp. 53−63
https://jnu.ac.bd/journal/portal/archives/science.jsp
ISSN 3005-4486 (Online), ISSN 2224-1698 (Print)

Influence of Y Substitutions on the Structural and Magnetic Properties of Mn-Zn Ferrites

Research Article

A. A. Momin[1,*], Anis Munshi[2], T. M. Imran[1], Amir Hossain[1], A. Mimi[1], M. A. Gafur[3], M. R. Hasan[4] and A. K. M. Akther Hossain[2]

[1]*Department of Physics, Jagannath University, Dhaka-1100, Bangladesh*

[2]*Department of Physics, Bangladesh University of Engineering & Technology, Dhaka-1000, Bangladesh*

[3]*Research Engineer, PP & PDC, Bangladesh Council of Scientific and Industrial Research (BCSIR)*

[4]*Materials Science Division, Atomic Energy Centre, BAEC, Dhaka-1000, Bangladesh*

DOI: https://doi.org/10.3329/jnujsci.v11i1.76693

Received: 17 January 2024, Accepted: 28 May 2024

ABSTRACT

The ordinary solid-state reaction method has been used to produce polycrystalline $Mn_{0.5}Zn_{0.5}Fe_{2-x}Y_xO_4$. X-ray diffraction (XRD) and scanning electron microscopy (SEM) have been used to study the structural and surface morphology of the samples, respectively. The formation of cubic spinel crystal structure is observed in XRD patterns. The Nelson-Riley function is used to determine the lattice parameters. Vegard's rule is followed by the lattice parameter change with Y content in different $Mn_{0.5}Zn_{0.5}Fe_{2-x}Y_xO_4$. The x-ray density, and the bulk density both increase with Y content due to the higher atomic weight of Y compared to atomic weight of Fe, as well as porosity decreases. SEM micrographs demonstrate that the average grain size decreases with the increase of Y contents. When x = 0.05, the initial permeability shows maximum then starts to decrease for further increase of Y content. For the composition $Mn_{0.5}Zn_{0.5}Fe_{1.95}Y_{0.05}O_4$, the relative quality factor (RQF) is found maximum (3477). With the increase of Y content, the peak value of the relative quality factor shifts to higher frequencies region which is the consequence of Snoek relation.

Keywords: *XRD, Microstructure, Initial permeability, Relative quality factor*

1. Introduction

Due to their practical significance in magnetic recording, catalysts, and magnetic fluids, polycrystalline spinel ferrites have attracted considerable interest in recent years (Peelamedu *et al*. 2003). The tetrahedral A-site and octahedral B-

***Corresponding Author:** A. A. Momin
E-mail: abdulla.al.momin@gmail.com

site with the AB_2O_4 crystal structure are present in these naturally formed super-lattices of ferrites. Based on the cation distribution in the chemical compositions, this material exhibits a wide range of magnetic characteristics. The magnetic characteristics of materials can be modified by substituting different cations into the *A* and *B*-sites. They can exhibit paramagnetic, ferrimagnetic, antiferromagnetic, glass and spin (cluster) properties, depending on the types of cations located in the *A*-site and *B*-site, respectively (Peelamedu *et al*. 2003; Hossain *et al*. 2007; Momin *et al*. 2017). As a result of their one-of-a-kind electronic and crystalline structure, spinel ferrites exhibit enhanced properties that make them suitable for use in a wide range of devices and systems, including transformers, inductors, recording heads, choke coils, antennas, *EMI* suppressors, deflection yokes, and power transformers (Arcos *et al.* 1998; Zapata A and Herrera G. 2013; Hossain *et al*. 2008; Sousa *et al*. 2001). Small, cheap, and high-performing electronic components are in significant demand due to the expanding mobile communication and *IT* industries. Because of their high reliability and performance, surface-mounting device (*SMD*) chip inductors are perfect for a wide range of applications These applications include low-voltage differential signaling, EMI suppression in USB, and other high-speed digital interfaces found in laptops, desktop computers, cameras, scanners, and other electronic devices (Stojanović *et al*. 2008). The chip inductors are made by co-firing after ferrite and electrical paste are coated alternately. Due to their wide range of uses in the electronics and telecommunications sectors, *Mn-Zn* ferrites are often regarded as an essential ceramic material. This is because they possess outstanding characteristics including higher initial permeability, higher saturation magnetization, higher resistivity, and minimal losses. The higher electric resistivity and higher magnetization are the two most significant properties of these materials. These properties depend on how the materials are made at the microscopic level. The process of preparation, condition during preparation, and the dopant are the responsible factors for controlling the microstructure (Yousuf *et al*. 2020; Chakrabarty *et al*. 2018; Maria *et al*. 2020; Verma *et al*. 2000; Tsay *et al*. 1997; Ewais *et al*. 2008; Dawoud and Shaat 2016). In inverse spinel ferrites, *Co, Ni, Fe* and *Cu* substituted in octahedral sites (*B* sites), have Curie temperature between 728K and 858K. It is well known that Curie temperature depends on the cation distributions. The 80% of *Mn* ions are occupy at *A* site and remaining 20% of *Mn* ions are occupy at *B* site. As a results, interaction between *A* sites *Mn* ion and *B* sites *Fe* ion are reduces which decreases the Curie temperature in the samples as *Fe* ions are occupy at both sites. In this case, *Mn* ions can be replaced by diamagnetic *Zn* ions as this substitution is not altered the cation distribution and may increase the saturation magnetization in the samples (Parekh K *et al*. 2006). Many researchers have taken numerous initiatives to increase magnetic properties of ferrites. Ramay *et al*. studied $Mn_{0.5}Cu_{0.5-x}Zn_xFe_2O_4$ compositions and got highest saturation magnetization for $Mn_{0.5}Zn_{0.5}Fe_2O_4$ samples (Ramay *et al*. 2014). Furthermore, many researchers synthesized $Mn_{0.5}Zn_{0.5}Fe_2O_4$ composition and studied its structural, magnetic and electric properties (Isfahani *et al*. 2009; Parekh K *et al*. 2000). It is widely known that $Mn_{0.5}Zn_{0.5}Fe_2O_4$ ferrite shows ferromagnetic behavior at room temperature. But nobody published *Y* ion substituted $Mn_{0.5}Zn_{0.5}Fe_{2-x}Y_xO_4$ ferrites with x = 0.00, 0.05, 0.10, 0.15, 0.20, 0.25, and 0.3. Our goal in this work is to determine the impact of small amounts of Y^{3+} on $Mn_{0.5}Zn_{0.5}Fe_{2-x}Y_xO_4$ ferrite concerning the fact that Fe^{3+} can be substituted by Y^{3+} from an octahedral *B*-site to a tetrahedral *A*-site, which significantly affects the sample parameters. A suitable material for magnetic use in the high frequency field may be introduced by this work.

2. Materials and method

2.1. Sample preparation

The flow chart for the sample preparation by solid-

state reaction technique is shown below:

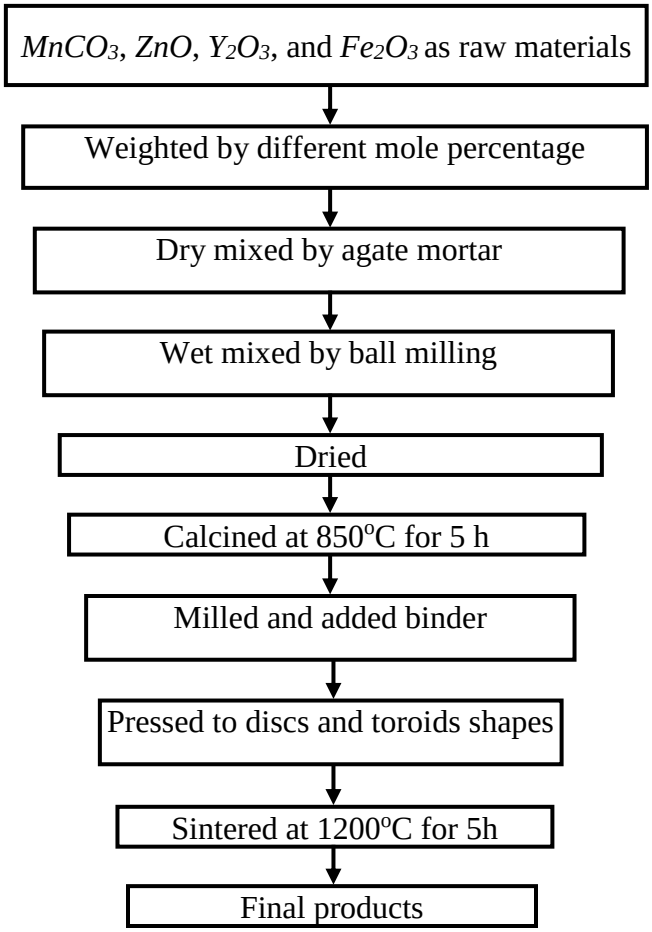

The $Mn_{0.5}Zn_{0.5}Fe_{2-x}Y_xO_4$ samples (for x = 0.00, 0.05, 0.10, 0.15, 0.20, 0.25, and 0.3) were prepared by solid-state reaction technique. As raw materials, high purity powders of $MnCO_3$, ZnO, Y_2O_3, and Fe_2O_3 were used. For the final synthesis of $Mn_{0.5}Zn_{0.5}Fe_{2-x}Y_xO_4$, stoichiometric proportions of the appropriate powders were well mixed before being calcined at 850°C for 5 hours. After utilizing polyvinyl alcohol as a binder to granulate the fine powders, samples in the shapes of discs and toroids are formed by applying pressure (7000 P.S.I.). Sintering was placed on the samples for 5 hours at temperatures of 1200°C in air. The ramps for heating and cooling throughout the sintering process were 10°C and 5°C per minute, respectively.

2.2. Characterizations

For structural analysis, X-ray diffractometer (D8-Advance Bruker) with CuK_α radiation (λ = 1.5418×10^{-10} m) is used. To determine each peak's lattice parameter, the following formula has been used:

$$a = d\sqrt{h^2 + k^2 + l^2} \qquad (1)$$

Where h, k, and l are represents the Miller indices of the crystal planes.

Nelson-Riley method has been used for determining each sample's lattice constant where Nelson-Riley function $F(\theta)$ is (Nelson and Riley

1945):

$$F(\theta) = \frac{1}{2}\left(\frac{cos^2\theta}{sin\theta} + \frac{cos^2\theta}{\theta}\right) \quad (2)$$

Where, θ represents the Bragg's angle.

The scanning electron microscope (SEM) has been used for analysing samples surface morphology. The equation that is used to determine the bulk density (ρ_B) of the samples is as follows:

$$\rho_B = \frac{m}{\pi r^2 t} \quad (3)$$

Where m represents the pellet's mass, r its radius, and t its thickness.

Using the following formula, the X-ray density of the specimens is determined:

$$\rho_x = \frac{nM}{N_A V}, \quad (4)$$

Where, N_A represents Avogadro's number, M represents the molar mass of the sample, as well as V and n represents the volume of the unit cell and the number of atoms in a unit cell, respectively. The porosity of each sample has been calculated using the following formula:

$$P(\%) = \frac{\rho_x - \rho_B}{\rho_x} \times 100 \quad (5)$$

For determining the real part of complex initial permeability ($\mu_i^{'}$), the following formula has been used:

$$\mu_i^{'} = \frac{L_S}{L_0} \quad (6)$$

Where, L_s is the sample core's self-inductance, and L_o is the inductance of the winding coil without the sample core. Where, L_o has been calculated geometrically using the formula:

$$L_o = \frac{\mu_0 N^2 S}{\pi \bar{d}} \quad (8)$$

Where N is the coil's turn count (N = 4), S is its cross-sectional area, and $\bar{d}$ is the toroidal sample's mean diameter (Zhang *et al*. 2012). The imaginary part of complex initial permeability has been calculated using the following formula:

$$\mu_i^{''} = \mu_i^{'} tan\delta_M \quad (9)$$

Where, $tan\delta_M$ indicates the magnetic loss of the samples.

3. Results and discussion

3.1. X-ray diffraction analysis

The *XRD* patterns for various $Mn_{0.5}Zn_{0.5}Fe_{2-x}Y_xO_4$ samples are shown in Fig. 1. The presence of cubic spinel structure of ferrite is confirmed by *XRD* patterns for each sample. All peaks are identified and well consistent with spinel ferrite's *JCPDS* peaks as well as with previous study (Hossain *et al*. 2004). Some extra peaks are available in *XRD* patterns which are due to formation of Fe_2O_3 (Hu P *et al*. 2010).

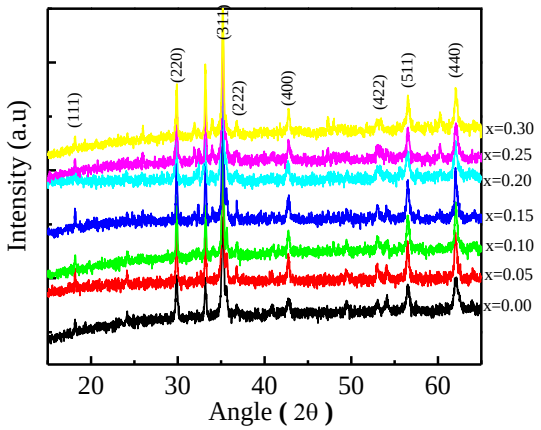

Fig. 1: The X-ray diffraction pattern of $Mn_{0.5}Zn_{0.5}Fe_{2-x}Y_xO_4$.

3.2. Lattice parameter and lattice constants

The Nelson-Riley function has been used to compute the values of lattice parameter (Nelson and Riley 1945). As can be seen in Fig. 2(a), the values of lattice parameter (a) of all the peaks for a sample are plotted against $F(\theta)$. Then for determining the precise value of lattice constant (a_0), the least square fit method has been used. For the given sample, the exact value of the a_0 is located where the straight line representing the least-squares fit meets the y-axis (i.e., at $F(\theta) = 0$) where the investigated samples contain $Mn_{0.5}Zn_{0.5}Fe_{2-x}Y_xO_4$. Consequently, the ionic radius of the variant ions for composition is then expressed as $r_{(variant)} =$

$xr_{(Y)} + (2-x)r_{(Fe)}$ (El Ata *et al*. 2005).

Here, $r_{(Y)}$ refers to the ionic radius of Y^{3+}, which is equal to 0.98Å, while $r_{(Fe)}$ refers to the ionic radius of Fe^{3+}, which is equal to 0.73 Å (Whittaker and Muntus 1970). The relationship between $r_{(variant)}$ with *Y* content is shown in Fig. 2(b), where it can be seen that $r_{(variant)}$ increases with the increasing of *Y* contents in the samples. Table-1 is a tabular representation of the measured values of each sample's lattice constant, density, and porosity.

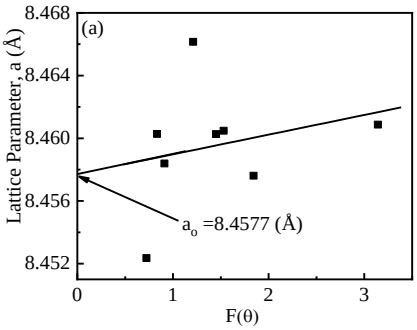

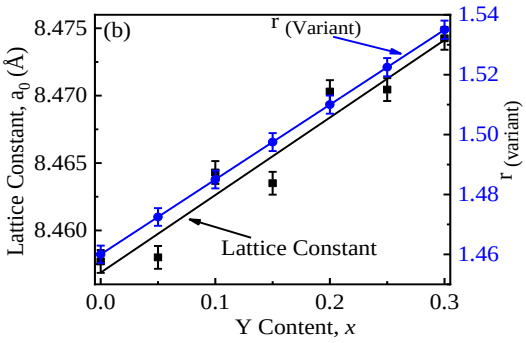

Fig. 2: (a) Variation of '*a*' with $F(\theta)$, and (b) variation of 'a_0' and $r_{(variant)}$ with Y content of $Mn_{0.5}Zn_{0.5}Fe_{2-x}Y_xO_4$.

Table 1: The a_0, ρ_x, ρ_B, *P*, $\bar{D}$, maximum *RQF* and μ_i' $Mn_{0.5}Zn_{0.5}Fe_{2-x}Y_xO_4$.

Compositions (*x*)	*a* (Å)	$\rho_x \times 10^3$ (kg/m^3)	$\rho_B \times 10^3$ (kg/m^3)	*P* (%)	$\bar{D}$ (μm)	$(RQF)_{max}$	μ_i'(at 10 kHz)
0.00	8.457	5.18	4.54	12.4	4.60	1513	184
0.05	8.458	5.21	4.63	11.1	4.14	3477	347
0.10	8.464	5.24	4.68	10.7	3.96	2012	220
0.15	8.465	5.28	4.74	10.2	3.81	809	98
0.20	8.470	5.30	4.78	9.8	3.61	707	71
0.25	8.471	5.34	4.81	9.6	3.57	547	37
0.30	8.474	5.36	4.90	8.9	3.51	455	27

The relationship between the change of the lattice parameter and the *Y* content in the samples has been obeyed Vegard's rule (Ramzan *et al*. 2021). It is also noticed from the Fig. 2(b) that the lattice constants increased with *Y* contents in the samples and it can be attributed due to the higher ionic radius of Y^{3+} compared to the ionic radius of Fe^{3+}.

3.3. Density and porosity

Fig. 3 demonstrates the variation of ρ_x, ρ_B, and *P* with *Y* contents for various $Mn_{0.5}Zn_{0.5}Fe_{2-x}Y_xO_4$.

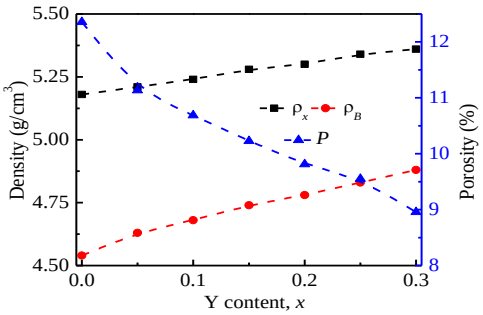

Fig. 3 Variation of ρ_x, ρ_B and *P* with *Y* content for

various $Mn_{0.5}Zn_{0.5}Fe_{2-x}Y_xO_4$.

From Fig. 3 it is shown that the values of ρ_x, ρ_B increase with the increase of *Y* contents while their corresponding property porosity decreased and it can be attributed due to the higher atomic weight of *Y* (88.90585 amu) compared to atomic weight of *Fe* (55.845 amu).

3.4. Microstructure

As micro-structure has significant effects on magnetic properties so it is important to study micro-structure of the samples. Fig.4 shows *SEM* images of various $Mn_{0.5}Zn_{0.5}Fe_{2-x}Y_xO_4$ compositions that were sintered at 1200°C. The linear intercept method is used to get the average grain size and it is denoted by $\bar{D}$ (Mendelson 1969). It has been seen that the average grain size reduces with the increase of *Y* contents. It is known that *Y* contents prevent the grain development in the samples (Ishaque *et al.* 2010) where yttrium oxide (Y_2O_3) forms at the grain boundaries and prevent the development of the grains. As well as the melting point of Y_2O_3 (2425°C) is higher than the melting point of Fe_2O_3 (1565°C) which decreases the $\bar{D}$ in the samples.

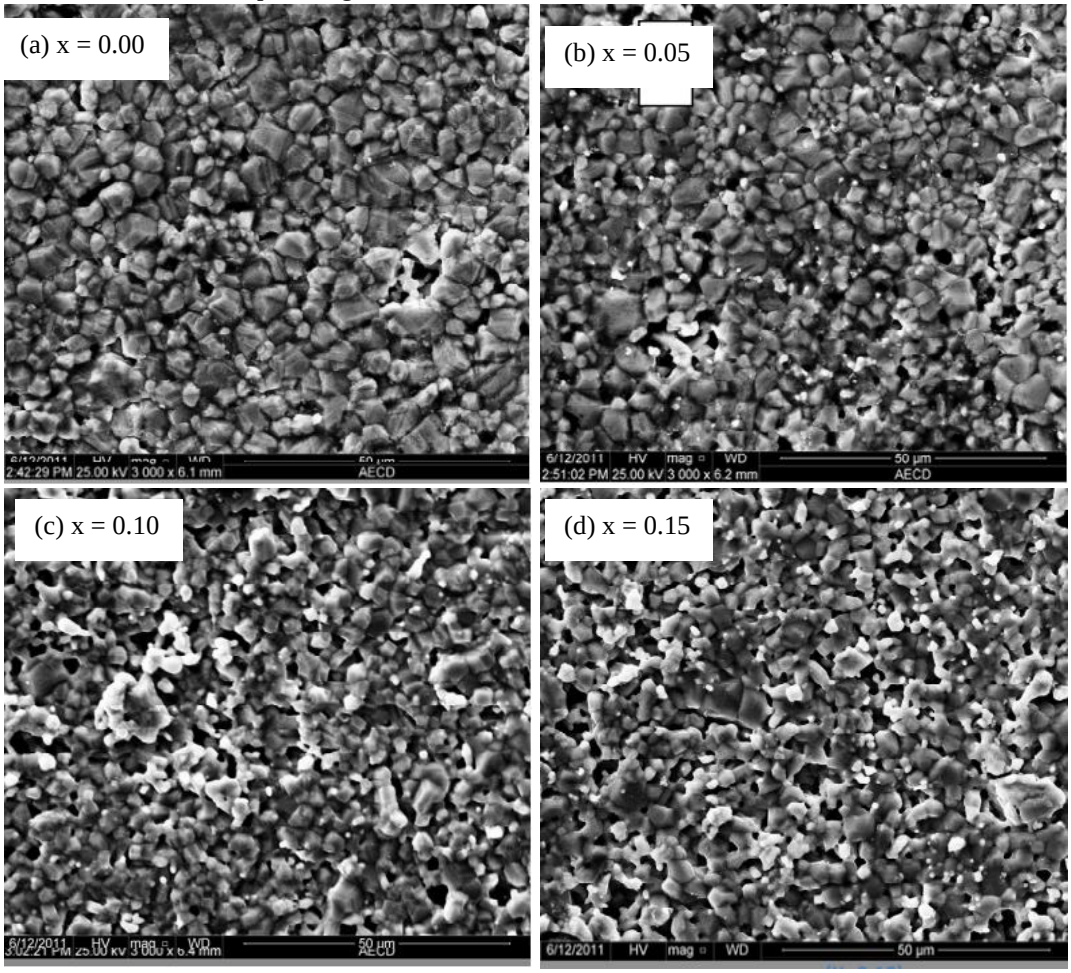

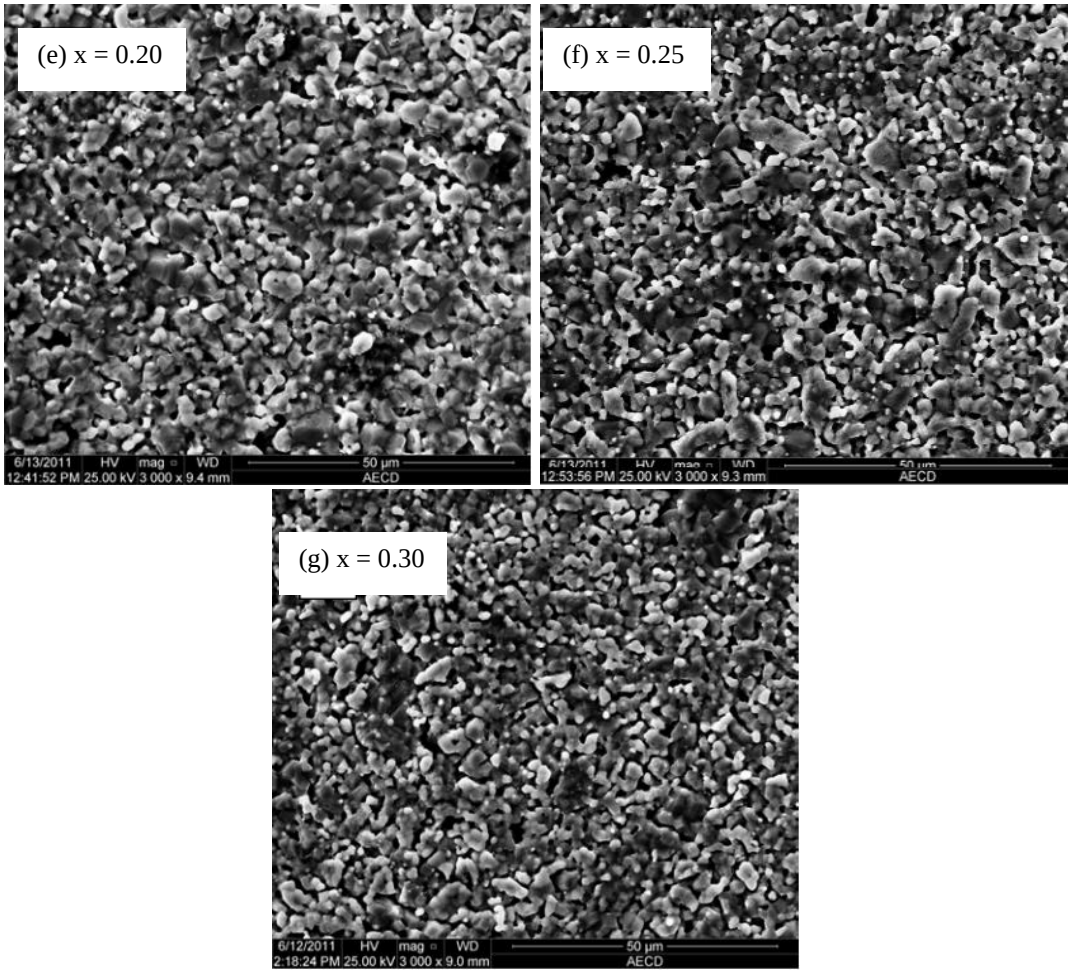

Fig. 4 SEM images of various compositions of $Mn_{0.5}Zn_{0.5}Fe_{2-x}Y_xO_4$ where, (a) x = 0.00, (b) x = 0.05, (c) x = 0.10, (d) x = 0.15, (e) x = 0.20, (f) x = 0.25, and (g) x = 0.30.

3.5. Complex initial permeability

The frequency dependence value of the μ_i' varies for various $Mn_{0.5}Zn_{0.5}Fe_{2-x}Y_xO_4$ samples are shown in Fig. 5(a). The μ_i' is found to be almost the same up to a certain frequency, and then reduces very rapidly at higher frequencies. This frequency at which the dispersion phenomena take place is referred to the resonance frequency (f_r) and it is assigned to either domain rotation or domain wall displacements or both (Rado *et al*. 1950; Nakamura 1997). This is the consequence of energy absorption which is the result of the oscillation frequency of the magnetic dipoles matching up with the applied frequency. Since the f_r of the samples with x = 0.25 and 0.30 are outside of the measurement frequency range, the values of μ_i' does not significantly changed throughout the whole frequency range. The Snoek's relation (Snoek 1948) states that the product of μ_i' and f_r is a constant for all ferromagnetic materials, with the formula $(\mu_i' - 1)f_r = \frac{\gamma}{2\pi M_s}$, where γ is the gyromagnetic ratio. It is widely known that polycrystalline

ferrite's permeability depends on spin rotation and domain wall motion (Sujatha *et al*. 2012). At lower frequency region, domain wall motion has more effect on permeability than spin rotation.

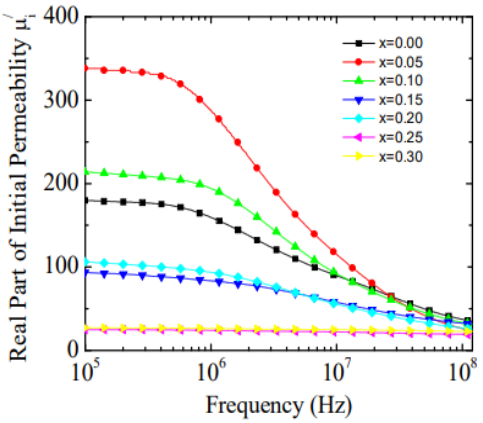

(a)

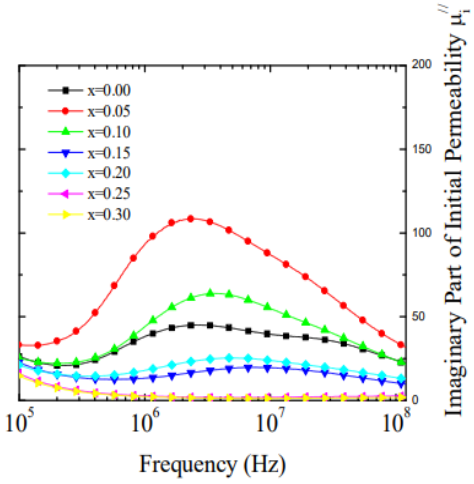

(b)

Fig. 5 The variation of (a) μ_i' and (b) $\mu_i''$with frequency for various $Mn_{0.5}Zn_{0.5}Fe_{2-x}Y_xO_4$.

The permeability that is caused by the motion of the domain walls is described by the following equation $\mu_i' \propto \frac{M_S^2 D}{\sqrt{K_1}}$, where K_1 represents the magnetocrystalline anisotropy constant and M_s represents the saturation magnetization (Chauhan *et al*. 2004). It has been shown that μ_i' increases as a result of an increase in the amount of *Y* substitution in the sample for x = 0.05 which can be attributed due to increasing of density in the samples. It is also found that further increase of *Y* contents in the samples, the value of μ_i' decreases which can be attributed due to the decreases of average gain size in the samples and average grain size is directly proportional to μ_i'. The decreasing trend of grain size increase resistance against domain wall motion due to increased number of grain boundaries. Therefore, initial permeability decreases with the decrease of grain size and increase of grain boundaries (Ishaque *et al.* 2015). However, at higher frequency region there is an increase in the intragranular pores trapped in the grains. These pores act as pinning centers for the domain wall movement consequently, domain wall movement is restricted and the μ_i' decreases (Nakamura T and Okano Y. 1996). The frequency dependence imaginary component of permeability (μ_i'') are displayed in Fig. 5(b). The μ_i'' appears due to a lag in domain wall motion relative to the applied alternating magnetic field. The figure indicates that all ferrites' μ_i'' values steadily rise with frequency except x = 0.25 and x = 0.30, reaching a broad maximum, when the real component of permeability rapidly declines. This phenomenon is commonly referred to as natural resonance (Snoek JL. 1948; Praveena K and Srinath S. 2014). According to Snoek's relation, we know that the product of initial permeability and resonance frequency, f_r, is always constant. From the relation we see that with the decrease of initial permeability, f_r increases. With the increase of Y content permeability decreases and according to snokes relation f_r increase. For the value of x = 0.25 and 0.30, f_r are out of measurement frequency range.

3.6 Relative quality factor

Fig.6 depicts the variation of *RQF* for various $Mn_{0.5}Zn_{0.5}Fe_{2-x}Y_xO_4$ samples as a function of

frequency i.e., (RQF $= \frac{\mu_i'}{tan\delta_M}$). For investigating the performance and perfection of the magnetic materials in the application, *RQF* is studied. It has been found that when the frequency is increased, the *RQF* first rises, then reaches a peak, and finally starts to fall for further increasing the frequency.

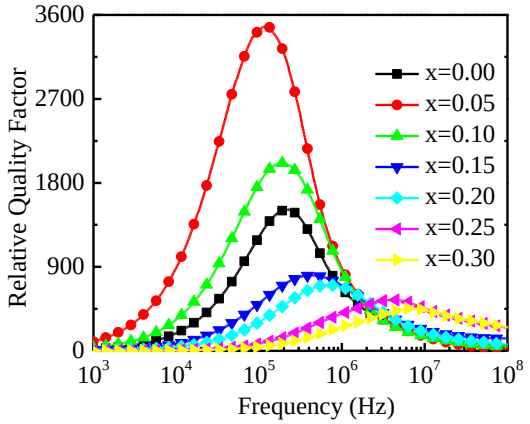

Fig. 6: The variation of *RQF* with frequency for various $Mn_{0.5}Zn_{0.5}Fe_{2-x}Y_xO_4$.

Peak in *RQF* is related with the ferromagnetic resonance that occurs inside the domains, and during the resonance, the largest amount of energy is transmitted from the externally applied magnetic field to the lattice, which causes the *RQF* to drop down very quickly. The value of *RQF* is maximum for x = 0.05 sample and for further increasing of *Y* contents in the samples the value of *RQF* decreases. The peaks of *RQF* are shifted to the higher frequency region with the increasing of *Y* contents in the samples which can be attributed due to the increasing resonance frequency in the samples with satisfying Snoek's relation (Snoek 1948).

4. Conclusions

XRD patterns of various $Mn_{0.5}Zn_{0.5}Fe_{2-x}Y_xO_4$ samples confirms the cubic spinel structure of ferrites. The lattice constants of the samples become larger as the amount of *Y* in the composition rises. The density of the samples increases with the *Y* contents in the samples and porosity decreased. The average grain size of the samples decreases with the increasing of *Y* contents. The μ_i' is maximum for x = 0.05 sample and then decreases for further increasing of *Y* contents. The $Mn_{0.5}Zn_{0.5}Fe_{1.95}Y_{0.05}O_4$ samples shows the maximum relative quality factor (3477) due to more perfection in its crystal structure.

Acknowledgment

The authors would like to express their gratitude to the CASR Grant number 288(23), BUET, Bangladesh for providing financial assistance for this study.

References

Arcos D, Valenzuela R, Vazquez M and Vallet-Regı M. 1998. Chemical homogeneity of nanocrystalline Zn–Mn spinel ferrites obtained by high-energy ball milling. *Journal of Solid-State Chemistry*, *141*(1), pp.10-16.

Chakrabarty S, Dutta A and Pal M. 2018. Effect of yttrium doping on structure, magnetic and electrical properties of nanocrystalline cobalt ferrite. *Journal of Magnetism and Magnetic Materials*, *461*, pp.69-75.

Chauhan BS, Kumar R, Jadhav KM, Singh M. 2004. Magnetic study of substituted Mg–Mn ferrites synthesized by citrate precursor method. *Journal of magnetism and magnetic materials* 283(1): 71-81.

Dawoud HA, Shaat SK. 2016. Initial Permeability and DC Conductivity of Cu–Zn Ferrite. *IUG Journal of Natural Studies* 14(1).

Denton AR, Ashcroft NW. 1991. Vegard's law. *Physical review A* 43(6): 3161.

El Ata AA, Attia SM, El Kony D, Al-Hammadi AH. 2005. Spectral, initial magnetic permeability and transport studies of $Li_{0.5-0.5x}Co_xFe_{2.5-0.5x}O_4$ spinel ferrite. *Journal of magnetism and magnetic materials* 295(1): 28-36.

Ewais EM, Hessien MM, El-Geassy AH. 2008. In-Situ synthesis of Magnetic Mn-Zn Ferrite ceramic object by solid state reaction. *J Aust Ceram Soc* 44: 57-62.

Goldman A. 2012. *Handbook of modern ferromagnetic materials* (Vol. 505). Springer Science & Business Media.

Hossain A.K.M. Akther., Mahmud ST, Seki M, Kawai T, Tabata H. 2007. Structural, electrical transport, and magnetic properties of $Ni_{1-x}Zn_xFe_2O_4$. *Journal of Magnetism and Magnetic Materials* 312(1): 210-219.

Hossain AKMA, Seki M, Kawai T, Tabata H. 2004. Colossal magnetoresistance in spinel type $Zn_{1-x}Ni_xFe_2O_4$. *Journal of applied physics* 96(2): 1273-1275.

Hossain AKMA, Tabata H, Kawai T. 2008. Magnetoresistive properties of $Zn_{1-x}Co_xFe_2O_4$ ferrites. *Journal of Magnetism and Magnetic Materials* 320(6): 1157-1162.

Hu P, Yang HB, Pan DA, Wang H, Tian JJ, Zhang SG, Wang XF, Volinsky AA. 2010. Heat treatment effects on microstructure and magnetic properties of Mn–Zn ferrite powders. *Journal of Magnetism and Magnetic Materials*, *322*(1), pp.173-177.

Isfahani MJN, Myndyk M, Menzel D, Feldhoff A, Amighian J and Šepelák V. 2009. Magnetic properties of nanostructured MnZn ferrite. *journal of Magnetism and Magnetic Materials*, *321*(3), pp.152-156.

Ishaque M, Islam MU, Khan MA, Rahman IZ, Genson A and Hampshire S. 2010. Structural, electrical and dielectric properties of yttrium substituted nickel ferrites. *Physica B: Condensed Matter*, *405*(6), pp.1532-1540.

Ishaque MAKM, Khan MA, Ali I, Khan HM, Iqbal MA, Islam MU and Warsi MF. 2015. Impacts of yttrium substitution on FMR line-width and magnetic properties of nickel spinel ferrites. *Journal of Magnetism and Magnetic Materials*, *382*, pp.98-103.

Maria KH, Akther US, Esha IN, Hossain MS and Khan MNI. 2020. Estimation of structural, electrical, and magnetic variations of Mn-Ni-Zn ferrites by substituting rare earth Y^{3+} for high-frequency applications. *Journal of Superconductivity and Novel Magnetism*, *33*, pp.2133-2142.

Mendelson MI. 1969. Average grain size in polycrystalline ceramics. *Journal of the American Ceramic society* 52(8): 443-446.

Momin, A.A., Parvin, R., Hossain A.K.M. Akther 2017. Structural, morphological and magnetic properties variation of nickel-manganese ferrites with lithium substitution. *Journal of Magnetism and Magnetic Materials*, 423: 124-132.

Nakamura T and Okano Y. 1996. Electromagnetic properties of Mn–Zn ferrite sintered ceramics. *Journal of applied physics*, *79*(9), pp.7129-7133.

Nakamura T. 1997. Low-temperature sintering of NiZnCu ferrite and its permeability spectra. *Journal of Magnetism and Magnetic Materials* 168(3): 285-291.

Nelson JB and Riley DP. 1945. An experimental investigation of extrapolation methods in the derivation of accurate unit-cell dimensions of crystals. *Proceedings of the Physical Society* 57(3): 160.

Parekh K, Upadhyay RV, Belova L and Rao KV. 2006. Ternary monodispersed $Mn_{0.5}Zn_{0.5}Fe_2O_4$ ferrite nanoparticles: preparation and magnetic characterization. *Nanotechnology*, *17*(24), p.5970.

Parekh K, Upadhyay RV, Mehta RV and Srinivas D. 2000. Electron spin resonance study of a temperature sensitive magnetic fluid. *Journal of Applied Physics*, *88*(5), pp.2799-2804.

Peelamedu R, Grimes C, Agrawal D, Roy R, Yadoji P. 2003. Ultralow dielectric constant nickel–zinc ferrites using microwave sintering. *Journal of materials research* 18(10): 2292-2295.

Praveena K and Srinath S. 2014. Dielectric and Magnetic Properties of $NiFe_{2-x}Bi_xO_4$ Nanoparticles. *Advanced Science, Engineering and Medicine*, *6*(3), pp.359-365.

Rado GT, Wright RW, Emerson WH. 1950. Ferromagnetism at very high frequencies. III. Two mechanisms of dispersion in a ferrite. *Physical Review* 80(2): 273.

Ramay SM, Rafique HM, Aslam S, Siddiqi SA, Atiq S, Saleem M, Naseem S and Shar MA. 2014. Structural, morphological, and magnetic characterization of sol-gel synthesized MnCuZn ferrites. *IEEE Transactions on Magnetics*, *50*(8), pp.1-4.

Ramzan R, Tariq M, Ashiq MN, Albalawi H, Ahmad I, Alhossainy MH, Ejaz SR, Khosa RY, Farid HMT, Khan HM and Al-Muhimeedh TI. 2021. Effect of yttrium ion on electrical and magnetic properties of barium-based spinel ferrites. *Journal of Materials Research and Technology*, *12*, pp.1104-1112.

Snoek JL. 1948. Dispersion and absorption in magnetic ferrites at frequencies above one Mc/s. *Physica*, *14*(4), pp.207-217.

Sousa MH, Tourinho FA, Depeyrot J, da Silva GJ, Lara MC. 2001. New electric double-layered magnetic fluids based on copper, nickel, and zinc ferrite nanostructures. *The Journal of Physical Chemistry B* 105(6): 1168-75.

Stojanović G, Srdić V, Maletin M. 2008. Electrical properties of yttrium-doped Zn and Ni–Zn ferrites. *physica status solidi (a)* 205(10): 2464-2468.

Sujatha C, Reddy KV, Babu KS, Reddy AR, Rao KH. 2012. Effects of heat treatment conditions on the structural and magnetic properties of MgCuZn nano ferrite. *Ceramics international* 38(7): 5813-5820.

Syue MR, Wei FJ, Chou CS and Fu CM. 2011. Magnetic, dielectric, and complex impedance properties of nanocrystalline Mn–Zn ferrites prepared by novel combustion method. *Thin Solid Films*, *519*(23), pp.8303-8306.

Tsay MJ, Tung MJ, Chen CJ, Liu TY. 1997. The manufacture of high permeability Mn-Zn ferrites by atmospherical protect. *Le Journal de Physique IV* 7(C1): C1-71.

Verma A, Goel TC, Mendiratta RG. 2000. Low temperature processing of NiZn ferrite by citrate precursor method and study of properties. *Materials science and technology* 16(6): 712-715.

Vocke RD. 1999. Atomic weights of the elements. *Pure and Applied Chemistry*1997 71(8): 1593-1607.

Whittaker EJ, Muntus R. 1970. Ionic radii for use in geochemistry. *Geochimica et Cosmochimica Acta* 34(9): 945-56.

Yousuf MA, Jabeen S, Shahi MN, Khan MA, Shakir I, Warsi MF. 2020. Magnetic and electrical properties of yttrium substituted manganese ferrite nanoparticles prepared via micro-emulsion route. *Results in Physics* 16:102973.

Zapata A and Herrera G. 2013. Effect of zinc concentration on the microstructure and relaxation frequency of Mn–Zn ferrites synthesized by solid state reaction. *Ceramics International*, *39*(7), pp.7853-7860.

Zhang S, Yao Y, Chen Y, Wang D, Zhang X, Awaji S and Ma Y. 2012. Effects of magnetic annealing on structure and multiferroic properties of pure and dysprosium substituted $BiFeO_3$. *Journal of Magnetism and Magnetic Materials* 324(14): 2205-2210.